https://doi.org/10.5194/egusphere-2024-663
Preprint. Discussion started: 7 March 2024


# Volcano Tsunamis and their effects on moored vessels safety: The 2022 Tonga event

Sergio Padilla[1], Íñigo Aniel-Quiroga[1], Rachid Omira[2,4], Mauricio González[1], Jihwan Kim[2], Maria A. Baptista[3,4]

[1] Environmental Hydraulics Institute, Universidad de Cantabria (IHCANTABRIA), Avda. Isabel Torres, 15, Santander, Spain

[2] Instituto Português do Mar e da Atmosfera (IPMA), Lisbon, Portugal

3 Instituto Superior de Engenharia de Lisboa; Lisbon, Portugal

4 Instituto Dom Luiz, Faculdade de Ciências da Universidade de Lisboa

*Correspondence to*: Sergio Padilla (sergio.padilla@unican.es)

**Abstract.** The violent explosion of the Hunga Tonga-Hunga Ha'apai volcano on January 15, 2022, was the origin of an atmospheric wave and a volcano-meteorological tsunami (VMT), both of which were recorded worldwide. The Tonga tsunami event caused resonance effects, leading to wave amplification in some far-field coastal areas like La Pampilla port in Callao, Peru, 10,000 km away from the volcano, where the rupture of the Vessel mooring lines occurred 15 hours after the eruption, resulting the spill of over 11,000 barrels of crude oil. This study aims to better understand the coastal effects of the Tonga tsunami, focusing on mooring loads in marine port environments. We examine how the VMT affected the safety of vessel moorings, hypothesising that atmosphere-induced acoustic ocean waves exerted hydrodynamic loading that endangered ships in port areas. A tsunami propagation obtained with a validated Boussinesq model at the local scale in Callao Bay provides the input to the mooring system model applied to a vessel with similar characteristics to the one docked at La Pampilla Port on the day of the Tonga event. This allows to study the effect of the VMT on overstressing and the potential mooring breakage. The results suggest that the Tonga tsunami event could be responsible for the movement and loss of positioning of the vessel. Furthermore, atmospheric waves significantly increased mooring stresses, particularly on the starboard quarter moorings. This event showed the need to prepare Tsunami Early Warning Systems and port authorities for detecting and managing VMTs induced by atmospheric acoustic waves. The work provides new insights into the far-field effects of the Tonga 2022 tsunami and discusses the lessons learned from such an uncommon event.

## 1. Introduction

Volcanic activity can trigger tsunamis through underwater explosion, caldera collapse, pyroclastic flow, flank collapse, or atmospheric gravity waves produced by large explosions (Paris, 2015). Throughout history, tsunamis of volcanic origin have been poorly studied due to their scarcity, leading to a limited understanding of their generation mechanisms and impacts at local, regional, and global scales (Hayward et al., 2022). To better understand this type of tsunami geneses and, therefore, reduce the epistemic uncertainties associated with it, several studies have been carried out (Antonopoulos, 1992; Pararas-Carayannis, 1992, 2004), which also include aquatic environments other than oceans, such as great lakes in Russia and The Philippines (Belousov et al., 2000; Falvard et al., 2018). In these studies, the 1883 eruption of the Krakatau volcano in the Sunda Strait (Indonesia), is commonly accepted as a main reference and a unique example (Kienle et al., 1987), as it was the first event of its kind recorded by different instruments worldwide (Paris et al., 2014; Yokoyama, 1981).

The Hunga Tonga-Hunga Ha'apai volcano (HTHH) is a submarine volcano near an island with the same name, and located 65 km NNW of the island of Tongatapu capital of Tonga, Nukuʻalofa (20.55°S, 175.39°W, see location in Figure 1). It is one of several active volcanoes in the Kingdom of Tonga, an archipelago nation in the South Pacific. The latest eruptive phase of the HTHH volcano began in mid-December 2021 with vigorous shallow-water explosive activity. On January 15, 2022, the volcano erupted at 4:00 a.m. UTC (Tonga Volcanic Eruption & Tsunami, 2022). Tonga experienced a volcano-meteorological tsunami (VMT) following a violent volcanic explosion that generated atmospheric gravity waves that propagated several times across the globe (Omira et al., 2022; Wright et al., 2022). These waves resulted from particle agitation in the atmosphere, travelling both vertically and horizontally at sonic and supersonic speeds (Kubota et al., 2022; Matoza et al., 2022; Wright et al., 2022; Dogan et al., 2023). Reports of ocean-free surface elevations greater than 1 m, causing damage to ports and infrastructure, emerged after the volcano explosion, originating from coastal areas near Tonga to the northwest and southeast Pacific (Ramírez-Herrera et al., 2022; Imamura et al., 2022). The affected locations include Australia, New Zealand, the United States, Mexico, and Peru, resulting in economic losses of approximately $102 million due to damages to floating docks, vessels, and infrastructure (Terry et al., 2022; World Bank, 2024).

The Tonga VMT was exceptional as it travelled at faster speeds than common tsunamis, had a global reach, affected the far-field coasts, and caused noticeable damages, human fatalities, and coastal hydrodynamic effects (Terry et al., 2022; Omira et al., 2022; Lynett et al., 2022). In their study, Omira et al. (2022) demonstrated that the primary source of the globally observed Tonga tsunami was the acoustic gravity waves radiated from the volcanic explosion. Here, the sizeable tsunami at some distant coasts (i.e., South America and Japan) was associated with the amplified ocean waves under Proudman resonance (Proudman, 1929) when the atmospheric wave propagated over very deep water (i.e., oceanic trenches). Other triggering mechanisms, including the submarine volcanic explosion, likely contributed to the generation of the locally observed tsunami in the far-field (Lynett et al., 2022; Omira et al., 2022).

The consequences of harbour-intruding long waves on moored vessels have been investigated by numerous studies (Ayca and Lynett, 2016, 2018, 2021; Kirby et al., 2022; Wilson et al., 2017). Seismic tsunamis often cause damage to port environments, such as broken moorings, collisions, or subsidence due to the large amount of momentum flux travelling within the harbour (Lynett et al., 2022; Ohgaki et al., 2008; Inoue et al., 2001). This also applies to tsunamis induced by atmospheric disturbances, which, like the previous ones, have caused damage to ships, moored vessels, and small bays (Imamura et al., 2022; Thomson et al., 2009). It has been observed in these studies that strong currents, often accompanying long-period waves, increase the probability of generating large catastrophes in harbours (Shigeki and Masayoshi, 2009; Sakakibara et

https://doi.org/10.5194/egusphere-2024-663
Preprint. Discussion started: 7 March 2024


al., 2010; Zheng et al., 2022; Lynett et al., 2012). Likewise, based on DOFs (Degrees Of Freedom), some authors such as López and Iglesias (2014) agree with the hypothesis that the motions in the vessel's horizontal plane (named roll, heave, and yaw) are strongly correlated with the total tsunami wave energy, with the currents being quite significant in ship sway response (Inoue et al., 2001). Furthermore, Ohgaki et al. (2008) and Zheng et al. (2022) mention that tsunamis are usually closer to the natural period of a mooring system (>80 sec), which makes these waves more prone to generate damage. Given the non-linearity of physical processes, it is pertinent to perform specific studies focused on each situation, configuration, and need (Zheng et al., 2022).

In La Pampilla Port in Peru, 10,000 km away from the Tonga volcano, the Italian-flagged oil tanker Mare Doricum reported the breakage of their mooring lines, 15 hours after the explosion of the HTHH volcano. The ship captain associated the breaking of the vessel's moorings with the abnormal waves in the sea, for which no warning was issued (SPDA Actualidad Ambiental, 2024). The Peruvian National Tsunami Warning System (CNAT) stated that the Tonga tsunami did not generate a tsunami on the Peruvian coast (CNAT, 2022). However, the tide gauge located in Callao Bay recorded a sudden change in sea level coincident with the time of the accident (Sea level station monitoring facility, 2022). This article addresses the impact of the Tonga 2022 tsunami on vessels moored on the Peruvian coast. It uses both sea-level data analysis and numerical modelling to improve the understanding of the damage caused by far-field Tonga VMT, studying its influence on the safety of moored vessels.

## 2. Data and Methods

Considering the complexity of the Tonga tsunami event, which likely involved multiple triggering volcanic mechanisms, analysing waves measured by both oceanic and atmospheric instruments is highly important (Wright et al., 2022). Firstly, we used the wavelet analysis to examine the composition of the signals recorded by both tidal gauges and DART buoys. Secondly, we studied the hydrodynamic effects of the Tonga tsunami in the far field, using tsunami numerical simulations (Boussinesq-type model) over high-resolution bathymetric models. Thirdly, we developed an analytical model to assess the stresses due to hydrodynamic loads on moored vessels.

### 2.1. Air pressure and sea level data

The data used in this study includes records from DART buoys, tide gauges, and weather stations in the Pacific Ocean. Figure 1 shows the location of the instruments considered in this study, with red circles representing the atmospheric pressure sensors, light blue triangles for the tide gauges, and yellow dots for the DART buoys.

The deep-water sea level time series (**D1**, **D2,** and **D3**) were obtained from the DART buoys, which in turn managed by the Center for Operational Oceanographic Products and Services of the National Oceanic and Atmospheric Administration (NOAA, https://www.ndbc.noaa.gov/). Coastal sea level data used in this study come from tidal stations connected in real-time to the Sea Level Station Monitoring Facility of UNESCO's Intergovernmental Oceanographic Commission (IOC, http://www.ioc-

https://doi.org/10.5194/egusphere-2024-663
Preprint. Discussion started: 7 March 2024


sealevelmonitoring.org/). The **B1** air pressure data have been obtained from local agents in New Zealand (NIWA, https://niwa.co.nz/) and those from stations **B3**, **B4**, **B5,** and **B8** came from the Dirección General De Aeronáutica Civil de Chile (DGAC, https://climatologia.meteochile.gob.cl/) through the Chilean Meteorological Office.

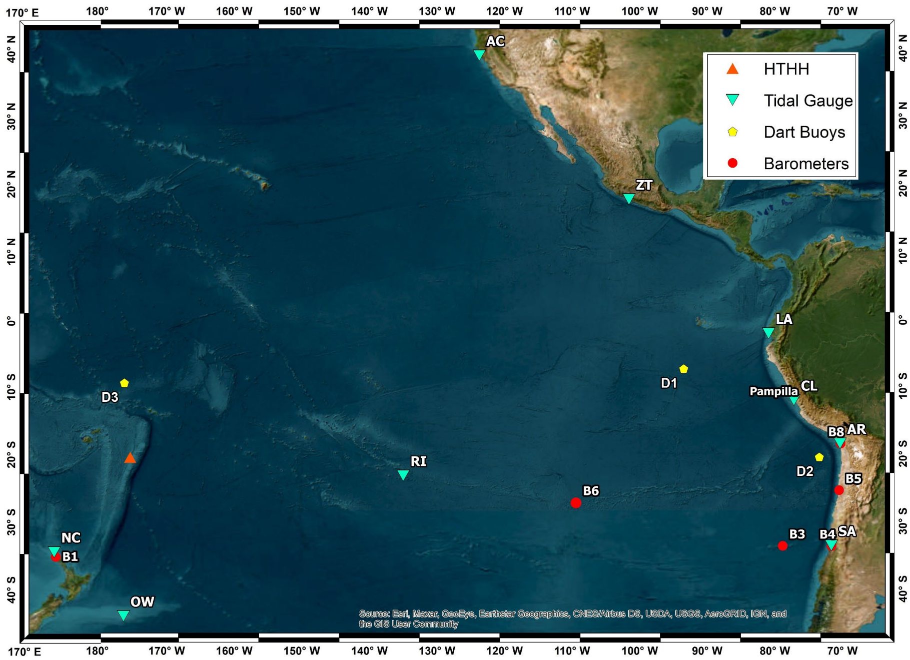


**Figure 1. Locations of the measuring instruments. Red circles show the atmospheric pressure sensors, the light blue triangles show the tide gauges, and the yellow circles refer to the Dart Buoys. The location of the Tonga volcano (HTHH) is the orange triangle.**

The sea level time series were de-tided using bandpass filters of 1.5 min-2.5 hours and 2 min - 3 hours for DART and tide gauge data, respectively, following Lynett et al. (2022). For atmospheric pressure data, a bandpass filter of 1.5 min - 2.5 hours was used (Table 1). Figure 2 shows the filtered time-series. The air-pressure time-series shows a notable peak of approximately 2 hPa with the "N-wave" pulse shape associated with the leading Lamb wave (Lynett et al., 2022; Omira et al., 2022).

| Type | ID | Name | Source (country) | Latitude (deg) | Longitude (deg) | Distance from source (km) | Sample (min) |
|---|---|---|---|---|---|---|---|
| Barometric | B1 | Nort Cape B. | New Zealand Gov | -35.134 | 173.263 | 1750 | 10 |
| | B3 | 330031 | Chilelan Gov. | -33.636 | -78.833 | 9110 | 1 |
| | B4 | 330030 | Chilelan Gov. | -33.656 | -71.613 | 9720 | 1 |
| | B5 | 250005 | Chilelan Gov. | -25.411 | -70.484 | 10230 | 1 |
| | B6 | 270001 | Chilelan Gov | -35.134 | 173.263 | 6530 | 1 |
| | B8 | 180042 | Chilelan Gov. | -18.513 | -70.266 | 10600 | 1 |

https://doi.org/10.5194/egusphere-2024-663
Preprint. Discussion started: 7 March 2024


| | | | | | | | |
|---|---|---|---|---|---|---|---|
| Tide Gauge | NC | North Cape T.G. | IOC (New Zealand) | -34.410 | 173.050 | 1715 | 1 |
| | RI | Rikitea | IOC (France) | -23.118 | -134.969 | 4025 | 1 |
| | AC | Arena Cove | IOC (USA) | 38.913 | -123.705 | 8700 | 1 |
| | ZT | Zihuatanejo | IOC (Mexico) | 17.637 | -101.558 | 9155 | 1 |
| | GL | Galapagos | IOC (Ecuador) | -0.752 | -90.307 | 9410 | 1 |
| | SA | San Antonio | IOC (Chile) | -33.582 | -71.618 | 9720 | 1 |
| | OW | Owenga | IOC (New Zealand) | -44.025 | -176.369 | 2290 | 1 |
| | AR | Arica | IOC (Chile) | -18.476 | -70.323 | 10595 | 1 |
| | CL | Callao | IOC (Perú) | -12.069 | -77.167 | 10240 | 1 |
| | LA | La Libertad | IOC (Ecuador) | 13.485 | -89.319 | 10305 | 1 |
| DART | D1 | 32413 | NDBC (USA) | -7.421 | -93.484 | 8800 | 15 |
| | D2 | 32401 | NDBC (USA) | -20.474 | -73.421 | 10205 | 15 |
| | D3 | 51425 | NDBC (USA) | -9.511 | -176.258 | 1530 | 15 |

**Table 1. Description of measuring instruments.**

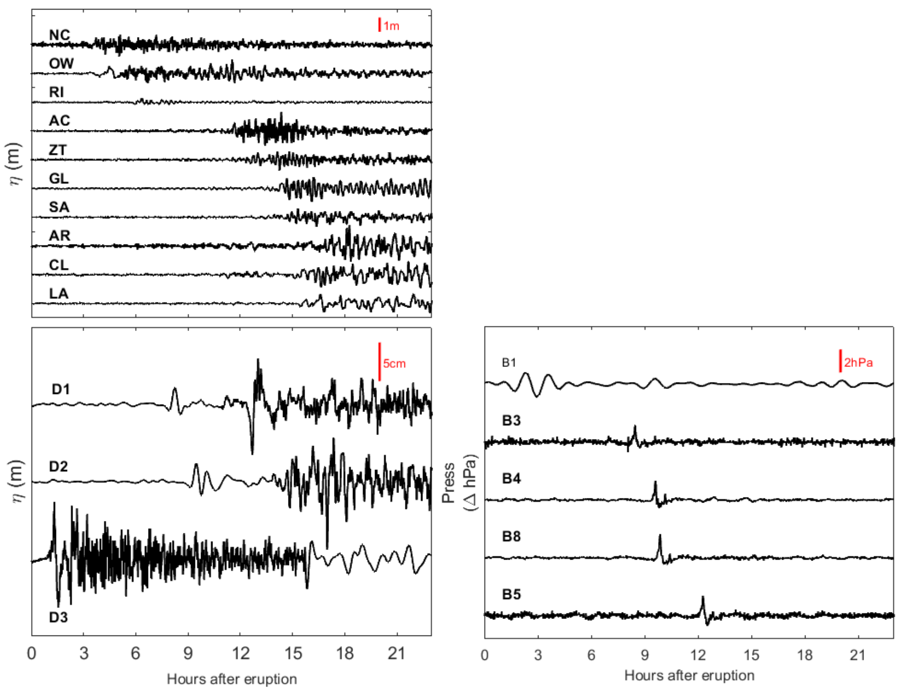


**Figure 2. De-tided time series. Air pressure data (right panel), tide gauge, and Dart data (left panel). Vertical red lines used to scale the magnitude of the variations in each instrument.**

https://doi.org/10.5194/egusphere-2024-663
Preprint. Discussion started: 7 March 2024


### 2.2. Spectral analysis

Spectral analysis is a practical tool for identifying the characteristic frequencies and energy levels in a time-series, particularly when it is composed of the superposition of signals with different frequencies. This method has found extensive application in the study of tsunamis (Abe, 2011; Rabinovich, 1997; Shevchenko et al., 2011; Satake et al., 2013; Baptista et al., 2016; Xu et al., 2022). In the time domain, we use wavelets to perform spectral analysis, allowing the estimation of the evolution of the spectral energy and, consequently, the first instants of energy increase for a given specific period.

### 2.3. Tsunami propagation model

Although air-ocean interaction has been recognized as a primary mechanism for the global fast-travelling Tonga 2022 tsunami (Omira et al., 2022), volcano-ocean interaction provided valid explanations for the near-field observation (Lynett et al., 2022; Pakoksung et al., 2022). As our primary target is Callao Bay, located approximately 10,000 km away from the HTHH volcano (Figure 3), we only focused on the tsunami induced by the atmospheric disturbances that followed the volcano explosion. The hypothesis of a point-source tsunami reaching the South American coast was ruled out considering the modelling results of a tsunami generated by the underwater explosion of the HTHH volcano (Omira et al., 2022).

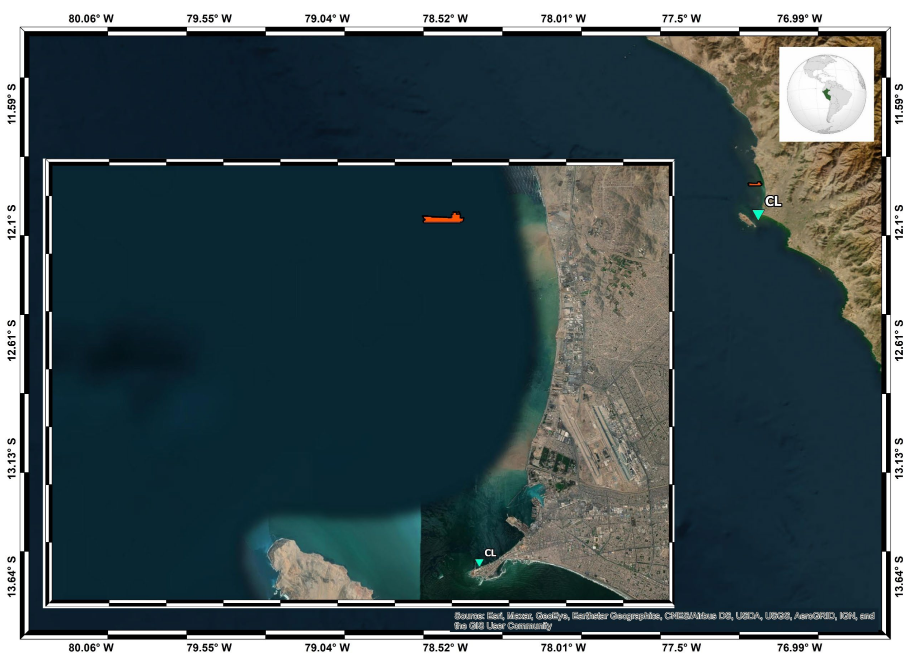


**Figure 3. Callao Bay and location of the vessel (Orange vessel) in the offshore port of La Pampilla, Peru.**

To simulate the VMT triggered by the explosion of the HTHH volcano, we used the finite volume GeoClaw code equipped with atmospheric pressure forcing terms that are handled using the flux-splitting method in momentum balance (Mandli and Dawson, 2014). This numerical code was validated in various

https://doi.org/10.5194/egusphere-2024-663
Preprint. Discussion started: 7 March 2024


meteotsunami studies (Kim and Omira, 2021; Kim et al., 2022; Omira et al., 2022). The determination of atmospheric source terms is based on barometric records from three distinct-selected observations in **B1**, **B6,** and **B8** (see Table 1 for details). We assumed the symmetrical propagation of atmospheric pressure from the source (HTHH volcano) at a constant speed of 310 m/s. Since a point source simulation on a sphere has two singularities (at the origin and antipode), we used a relaxation method as described in Omira et al. (2022).

Initially, our computational domain is between 40°S to 40°N and 170°E to 65°W, with a coarse bathymetry resolution of 1 degree, as obtained from GEBCO (https://www.gebco.net/). To achieve a finer spatial representation of the study area (i.e., Callao Bay), we employed four levels of refinement with resolutions of 1°, 1°/5, 1°/30, and 1º/2, using an adaptive mesh refinement (AMR), with a maximum refinement level of 3 across the entire domain. The full resolution of approximately 800 meters was reinforced near Callao Bay with local higher-resolution bathymetry data (GEOGPS PERÚ, https://www.geogpsperu.com/). To account for the bottom friction, GeoClaw software uses Manning's formulation, and the Manning coefficient of 0.02 was considered in this work. Our simulations were conducted using the Madsen's Boussinesq-type equations, with a constant value of B = 1/15 (Kim et al., 2017; Madsen and Sørensen, 1992).

The computation was performed on Intel Core i7-8700 CPU 3.2GHz using 10 cores corresponding to 1161 hours of propagation time, and 119 hours of wall time.

### 2.4. Stresses in moored ships model

Here, we use an analytical model to estimate the loads on a vessel's mooring system under the hydrodynamic effects of a tsunami (Tahar and Kim, 2004; OCIMF, 2010). The vessel is modelled as a rigid body with six degrees of freedom (DOFs). The first three DOFs are the surge, sway, and heave ($x$, $y$, and $z$) of the vessel's centre of gravity ($C_{OG}$), given in the global frame (Figure 4). The other three are the Euler angles, roll, pitch, and yaw ($\alpha$, $\beta$, and $\gamma$), which describe the local frame rotation status with respect to the global frame.

We considered two reference frames, the first of which is a global orthogonal inertial frame (fixed) with its origin located somewhere at the mean water level, where the X-axis points eastward and the Z-axis points upward for the global frame. The second is an orthogonal non-inertial frame, moving with the vessel, with its origin located at the $C_{OG}$. The X-axis points toward the bow while the Z-axis points upward for the local frame. The roll and pitch initial equilibrium positions are considered at zero degrees.

https://doi.org/10.5194/egusphere-2024-663
Preprint. Discussion started: 7 March 2024


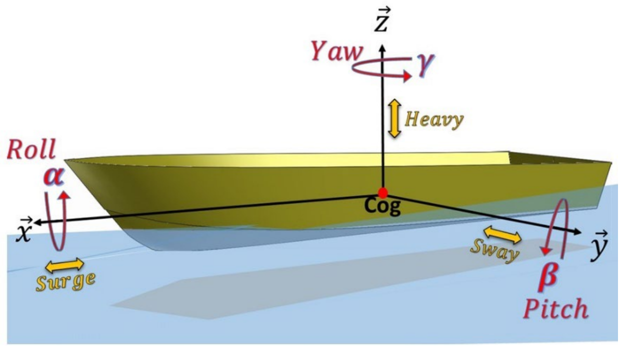


**Figure 4. Definition of Ship Motions in Six Degrees of Freedom, the yellow ones describe translation and the red ones rotation.**

The model contemplates the vessel's hydromechanics and physics characteristics such as hydrostatic stiffness (which considers both buoyancy and gravity forces), vessel mass $(m)$, metacentric heights $(GM_{t,l})$, and inertial forces defined by the vessel's moments of inertia around the principal axes $(I_{x,y,z})$ as well as describing the vessel's stability (Journée and Massie, 2001). The vessel's dynamics are described with the equations of a forced and damped mass-spring system which allows the following initial value problem (Eq. 1):

$$\begin{cases} \dot{\boldsymbol{Y}} = \boldsymbol{f}(\boldsymbol{Y},\boldsymbol{t}) = \begin{bmatrix} \dot{\xi} \\ \ddot{\xi} \end{bmatrix} = \begin{bmatrix} \dot{\boldsymbol{\xi}} \\ M^{-1} \cdot [B \cdot \dot{\xi} + G \cdot (\xi - \xi_0(t)) + F_m(\xi) + F_d(\xi, t)] \end{bmatrix} \\ \boldsymbol{Y}(\boldsymbol{t} = \boldsymbol{0}) = \boldsymbol{Y_0} \end{cases} \tag{1}$$

where $Y_0$ is the initial vessel state vector, containing the initial position and the speed of the vessel, $B$ is the damping matrix, $G$ is the stiffness matrix, ξ is defined as the stacking of all the DOFs, $\xi_0$ is the initial equilibrium position, and $F_m$ and $F_d$ are the mooring system forces and the current drag forces (Figure 5).

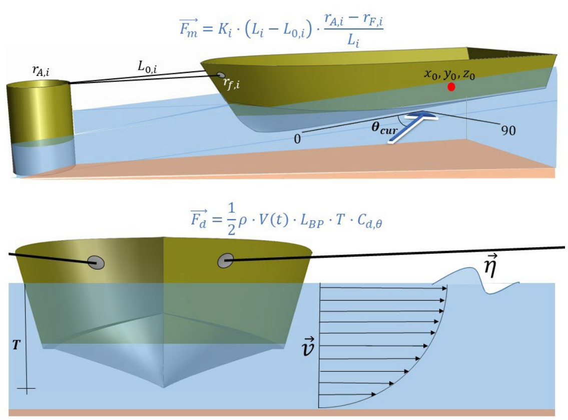


**Figure 5. Schematic layout of Ship Mooring system forces $F_m$ and Drag Forces $F_d$. The dynamics of the moored vessel are defined with a second-order ordinary differential equation (ODE)**

https://doi.org/10.5194/egusphere-2024-663
Preprint. Discussion started: 7 March 2024


The mooring system $\boldsymbol{F_m}$ is exclusively considered when the movement of the vessel results in a greater increase in the length of the line $L_i$ compared to the previous position, as shown in the following Eq. (2):

$$F_{m,i} = \begin{cases} K_i \cdot \left(L_i - L_{0,i}\right) \cdot \frac{r_{A,i} - r_{F,i}}{L_i}, & L_i > L_{0,i} \\ 0, & L_i > L_{0,i} \end{cases} \tag{2}$$

Where $K_i$ includes Elastic properties for the i-th line, $L_i$ is the line length, $r_A$ and $r_F$ are the pile and fairlead positions (where the line is tied to the hull). The Morison drag force model (Oh et al., 2020) is utilized to calculate the drag force $F_d$. The tsunami current at time $t$ is defined by its speed. The current drag force changes depending on the angle of incidence, the $F_{d,x,y}$, calculated as Eq (3):

$$\boldsymbol{F_{d,x,y}(\xi, t) = \frac{1}{2}\rho \cdot V(t) \cdot L_{BP} \cdot T \cdot \begin{pmatrix} \cos(\gamma) & -\sin(\gamma) \\ \sin(\gamma) & \cos(\gamma) \end{pmatrix} \cdot \begin{pmatrix} C_x(|\theta(t)|) \\ C_y(|\theta(t)|) \cdot sgn(\theta(t)) \end{pmatrix}} \tag{3}$$

Where $C_x$ and $C_y$ are the drag forces in the $x$ and $y$ axes, $\rho$ is the water density, $V(t)$ is the tsunami current velocity, $L_{BP}$ is the length between the perpendicular, T is the vessel's draft, and $\gamma$ is the Yaw DOF. We considers the tsunami current angle $\theta$ to be parallel to the vessel's centerline at zero degrees. Finally, this first-order ODE is integrated with a Runge-Kutta-4-5 method implemented in the SciPy Python library (Dormand and Prince, 1980; Shampine, 1986).

The model inputs consist of the vessel's dimensions, hydromechanical and mass properties, the ship's berthing scheme (including piles and fairleads coordinates), the line properties (such as young modulus and length), and the temporal tsunami dynamics (including waves and currents time-series) at the vessel's location. The model outputs the movements in each DOF and the resulting stress, measured in tons, for each line throughout the time series.

# 3. Results

## 3.1. Atmospheric and oceanic data analysis

The analysis using wavelets is based on the hypothesis that the atmospheric waves' integral characteristics, such as the periods and propagation velocities, remain reciprocal when resonance is generated between atmospheric and oceanic waves. This allows the current knowledge extrapolation about atmospheric waves, which have been extensively studied in the literature, and their effect on oceanic tsunami waves.

The results in Figure 6, Figure 7, and Figure 8 show the analysis of the recorded atmospheric and sea-level signals, which are composed of three panels for each sensor. The top panel shows the filtered time-series of both sea level and atmospheric pressure (blue and orange respectively). The orange arrow indicates the leading Lamb wave arrival time respectively. The lower panel shows the spectral results (wavelets) of the de-tided series of the ocean surface, the red-blue color scale marks the highest and lowest energy concentrations respectively; to the right is the Fourier spectrum obtained from integrating the wavelet over time.

https://doi.org/10.5194/egusphere-2024-663
Preprint. Discussion started: 7 March 2024


Results in Figure 6 correspond to the tide gauges **NC**, **OW**, and **RI**, DART buoy **D3**, and pressure sensor **B1** (see Figure 1 for location). Wavelets consistently show four energy groups for sensors tide gauges **NC, OW, RI**, and DART buoy **D3**. These results allows for the identification of the initial characteristics of tsunami waves forced by atmospheric waves, i.e., the arrival times and wave periods.

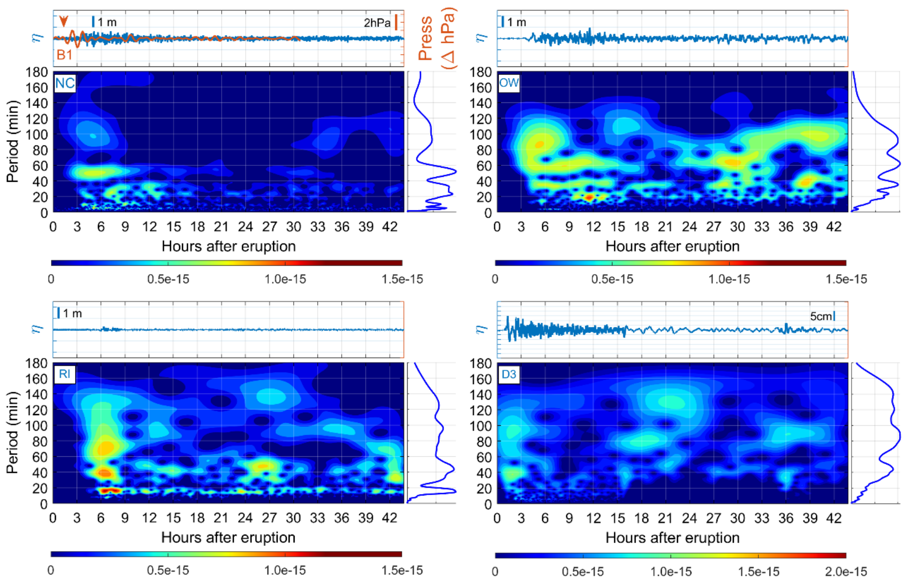


**Figure 6. Analysis of air-pressure and sea-level records at tide gauges NC (North Cape, New Zealand), OW (Owenga, New Zealand) and RI (Rikitea, France), DART buoy D3 (51425, NDBC), and air-pressure sensor B1 (North Cape, New Zealand). For each sensor, the time series of the air-pressure sensor (orange line) and tide gauge (blue line) are shown in the upper panel. The orange arrow refers to the arrival time of the leading pressure pulse. The panel to the right of the wavelet is the resulting frequency spectrum (FFT) of the time integration of the wavelet.**

The energy clusters fall within the 5-10 min, 20 to 40 min, 40 to 60 min, and 80-120 min periods, do the energy clusters suggest that there were multiple mechanisms that generated the Tonga tsunami waves. These results are consistent with the findings of previous studies (Hu et al., 2023; Kubota et al., 2022; Omira et al., 2022). The manometer station **B1** and tide gauge **NC** allow the estimation of the propagation velocities of the atmospheric disturbances as approximately 324 m/s.

Figure 7 shows far-field results (deep waters near the Peruvian coast) in sensors **D1-B3** and **D2-B5**. Air-pressure time-series shows the 2 hPa pulse associated with the leading Lamb wave arrived first, followed by second disturbances travelling at more than 200 m/s (Hu et al., 2022; Omira et al., 2022). DART buoy wavelets provide more spectral information related to the physical properties of these atmospheric waves coupled in the ocean. For example, DART Buoy **D2** shows that the first pulse coincides with the leading Lamb wave between 30- and 60- minute periods arriving 9 hours after the main eruption. Then, there is a group of energy contained in four ranges of periods: (i) about 10 min, (ii) between 20 and 40 min, (iii) between 60 and 90, and (iv) between 100 and 140 min. The latter is possibly associated with the air-ocean

https://doi.org/10.5194/egusphere-2024-663
Preprint. Discussion started: 7 March 2024


Proudman resonance that occurred on the Tonga Trench and propagated as common tsunami gravity waves towards the Southern American coast (Omira et al., 2022).

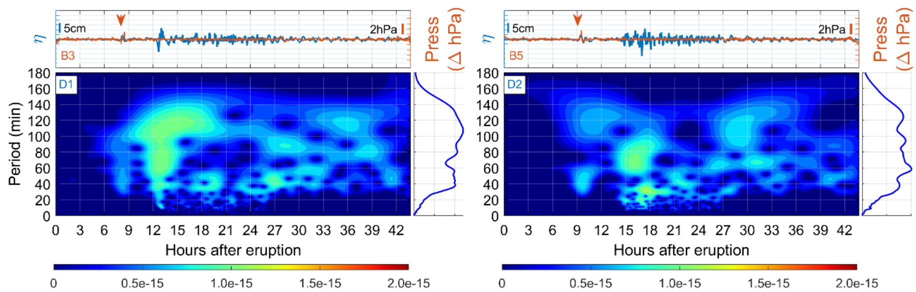


**Figure 7. Analysis of air-pressure and sea-level records at DART buoys D1 (32413, NDBC) and D2 (32401, NDBC) and atmospheric pressure sensors B3 (330031, Chile) and B5 (250005, Chile). For each sensor, the filtered time series of the atmospheric pressure sensor (orange line) and tide gauge (blue line) are shown in the upper panel. The orange arrow refers to the arrival of the leading pressure pulse. The right panel of the wavelet is the frequency spectrum resulting from the time integration of the wavelet.**

Figure 9 shows the spectral results for other locations along the Pacific American coasts. The South Pacific American instruments are **SA-B4** (Chile), **AR-B8** (Chile), **CL-B5** (Peru) and **AL** (Ecuador). The sensors in Central and North America are **ZT** (Mexico) and **AC** (USA). The wavelets' results in Chile, Mexico, and the USA show several energy groups: one in 40 - 60 min periods, another group between 20 - 40 min, and finally, energy in periods less than 10 min. Those wavelets exhibit a pattern similar to that observed in deep water sensors, with a notable difference regarding the absence of periods close to 120 min.

Subsequently, Figure 8 shows the analysis for sensors **LA** (Ecuador), **CL-B5** (Peru), 15 km from the vessel accident. The black dotted vertical line on the **CL** wavelet refers to the moment when the ship's moorings break and the oil spill occurs, according to the captain of the ship Mare Doricum. It can be observed in the **CL** wavelet that: (i) the Lamb wave coupled in the ocean (spectral energy between 30 - 60 min periods), (ii) the mooring break moment coincides with the high period spectral energy (max between 110-130 min period). Additionally, the energy within the 100 to 140 min period is present in deep water, (e.g., at DART buoy **D1** in Figure 4) and amplified exclusively in front of the Ecuador and Peru coasts (**LA** and **CL** tide gauges).

https://doi.org/10.5194/egusphere-2024-663
Preprint. Discussion started: 7 March 2024


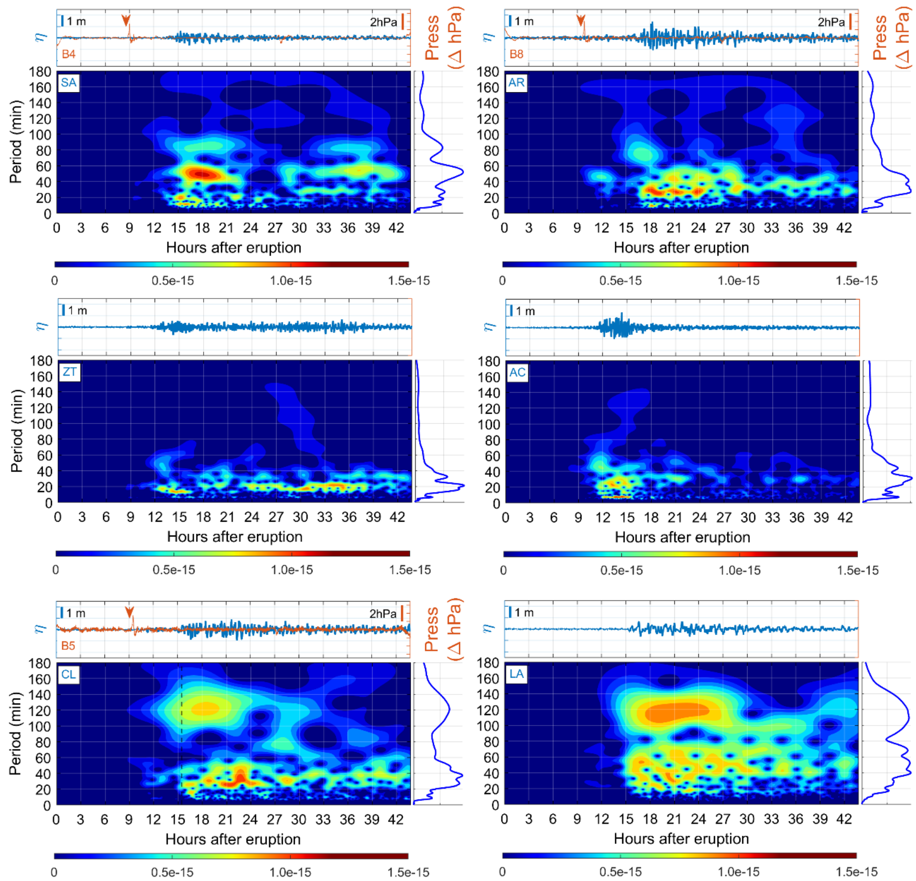


**Figure 8. Analysis of air-pressure and sea level records at the tide gauges of SA (San Antonio, Chile), AR (Arica, Chile), ZT (Zihuatanejo, Mexico), AC (California, USA), CL (Callao, Peru), and LA (La Libertad, Ecuador). The upper panel shows the time series of the atmospheric pressure sensor (orange line) and tide gauge (blue line). The orange arrow refers to the arrival of the leading Lamb wave. For the lower panel, we have the Wavelet. The vertical black dashed line in the CL wavelet refers to the instant when the vessel's moorings broke at La Pampilla port, Peru. The panel to the right of the wavelet is the frequency spectrum.**

### 3.2. Numerical modelling of atmospheric pressure-induced tsunami waves

The numerical simulations have been calibrated/validated using both far- and near-field instrumental data. After validation, the significance of tsunami-like waves induced by atmospheric acoustic-gravity waves and tsunami-induced waves resulting from the submarine explosion were analyzed. We present the results in Figure 9, which shows the observed and simulated tsunami waveforms near the coast of Peru.

A comparison of observed and simulated tsunami waveforms at DART buoys (**D1** and **D2)** shows that the Boussinesq numerical model correctly reproduces the first tsunami wave. It also fairly reproduces the second train of tsunami waves, likely associated with air-ocean resonance in deep ocean (near Tonga trench), and travelling at common tsunami speeds (Omira et al., 2022; Hu et al., 2023; Kubota et al., 2022). In shallow waters, the model correctly reproduces the tide gauges **LA** and **CL** (closest to the port of La

https://doi.org/10.5194/egusphere-2024-663
Preprint. Discussion started: 7 March 2024


Pampilla in Peru.), like in deep waters. It is interesting to note that the model succeeded in correctly reproducing the 120-minute long-period wave (also observed in deep water).

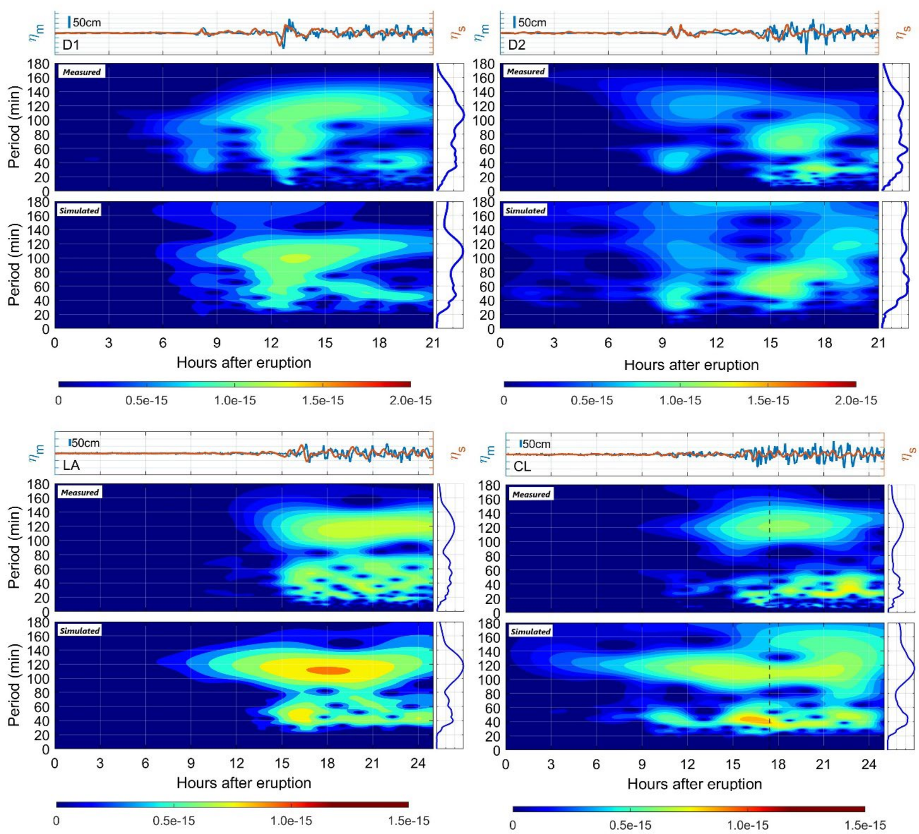


**Figure 9. Validation of numerical results at DART D1 and D2 buoys and tide gauges CL (Callao, Peru), and LA (La Libertad, Ecuador). For each buoy, the measured (blue line) and simulated (orange line) time series are shown in the upper panel. The lower panel shows the measured free sea surface wavelets (upper wavelet) and numerical simulation (lower wavelet). The vertical black dashed line in CL refers to the instant of the vessel mooring break in La Pampilla harbor, Peru. The panel to the right of each wavelet is the frequency spectrum.**

In general, an adequate VMT simulation is achieved, then the wavelets and Fourier transform show a correct trend of the wave characteristics measured in each sensor, as shown in Figure 9. Wavelets corresponding to both deep and shallow waters present several groups of waves forced by acoustic waves between 20-40 minutes, periods 40-60 min, and long-period waves about 120 min (Hu et al., 2023; Kubota et al., 2022; Omira et al., 2022). Likewise, the Fourier spectra also show two distinguished groups of 40-60 min and 100-120 min in shallow water.

Compared to the DART buoys, the simulations exhibit similar behaviours because they are located at great depths, where the influence of the bathymetry and the land boundaries is negligible. The simulations demonstrate that tide gauges reveal variations such as earlier arrival times or more energy, possibly

https://doi.org/10.5194/egusphere-2024-663
Preprint. Discussion started: 7 March 2024


associated with local effects and limitations in resolution. However, the model's results are similar to the measured data.

Figure 10 displays simulation results for shallow water tide gauges **GL** and **SA** (located north and south of Peru, respectively), demonstrating that the 120-minute period wave is exclusive of the coast of Peru and is likely intensified by local effects. The wavelet analysis indicates that neither the simulated nor the measured waves show a significant amplification of high-period energy, as seen in the sensors situated off the coast of Peru.

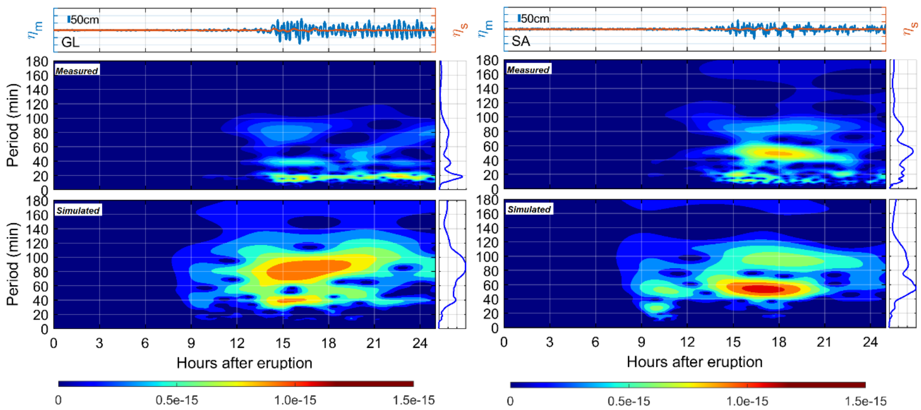


**Figure 10. Comparisons of the numerical results at the GL (Galapagos, Ecuador) and SA (San Antonio, Chile) tide gauges are shown. For each tide gauge, the measured (blue line) and simulated (orange line) time series are shown in the upper panel. The lower panel has measured (upper wavelet) and simulated (lower wavelet) ocean results. The panel to the right of each wavelet is the frequency spectrum.**

### 3.3. Vessel response due to acoustic and tsunami waves

The model described in Section 2.4 was implemented to estimate the mooring stresses due to tsunami hydrodynamic effects produced during the Tonga event. The purpose is to demonstrate the variability in stress levels when exposed to tsunami waves of varying periods and, therefore, different hydrodynamic conditions.

The current velocity and water elevation time-series were extracted from the Boussinesq tsunami model, presented in Section 2.3 and validated in Section 3.2 at coordinates 11º56' **S**,77º11' **W**, the location of Terminal 2 of La Pampilla port (as shown in Figure 3). Figure 11 describes the mooring scheme. Each pile is defined as immovable to focus stresses on every line. The scheme is similar to the one found in Terminal 2 of the Port of La Pampilla in Peru during the mooring-break accident.

https://doi.org/10.5194/egusphere-2024-663
Preprint. Discussion started: 7 March 2024


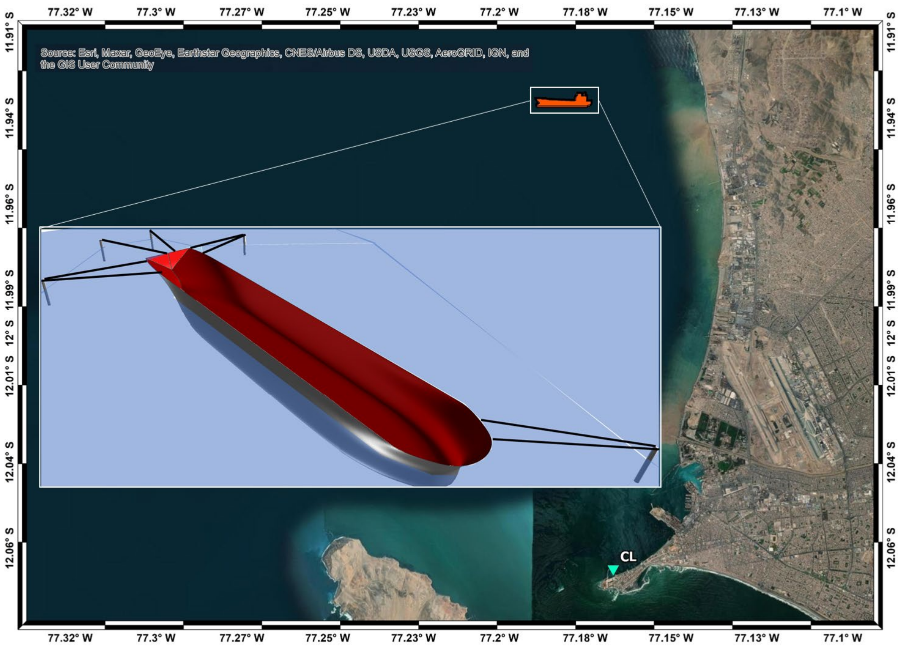


**Figure 11. La Pampilla port location (square in left map) and berthing scheme implemented in the mooring lines stress model (right panel).**

In Tables 2 and 3 presents the vessel's description and its hydromechanical characteristics. The entire mooring system schematic and the data used in the model are provided. The vessel used in this study is not the oil tanker Mare Doricum, but rather one with comparable physical characteristics. The vessel is moored to five buoys with eight moorings, one forward and four at the stern (in addition to two stern anchors anchored at a depth of 18 meters). The ship is considered fully loaded throughout the simulation. (Figure 12).

| | | |
|---|---|---|
| LOA | 274 | m |
| Beam | 48 | m |
| draft | 8 | m |
| Mass | 119.311 | Ton |
| Xcg | 118.3 | m |
| Ycg | 0 | m |
| Zcg | -6.65 | m |
| Ixx | 21470000 | Ton m2 |
| Iyy | 515780000 | Ton m2 |
| Izz | 515780000 | Ton m2 |
| MGt | 20.042 | m |
| MGl | 471.824 | m |
| Displacement | 100,434 | Ton |

https://doi.org/10.5194/egusphere-2024-663
Preprint. Discussion started: 7 March 2024


| | | |
|---|---|---|
| Waterplane area | 9920.68 | m2 |
| Gz | 99949.56131 | Ton m |
| Groll | 2012895.542 | Ton m |
| Gpitch | 47387108.39 | Ton m |

**Table 2. Description of the vessel used in the mooring stress simulation**

| Line number | Pile position $r_{A,i}$ (m,m,m) | Fairlead position $r_{f,i}$ (m,m,m) | Length $L_{0,i}$ (m) |
|---|---|---|---|
| 0 | (208.27, 80.13, 3.00) | (138.34, 5.65, 6.00) | 103.21 |
| 1 | (208.27, 80.13, 3.00) | (121.00, 13.42, 6.00) | 115.78 |
| 2 | (-152.09, 96.13, 3.00) | (-85.20, 24.30, 6.00) | 105.64 |
| 3 | (-152.09, 96.13, 3.00) | (-92.13, 23.61, 6.00) | 103.54 |
| 4 | (-220.98, 25.94, 3.00) | (-118.19, 3.57, 6.00) | 107.30 |
| 5 | (-225.43, -57.61, 3.00) | (-117.98, -4.43, 6.00) | 125.63 |
| 6 | (-184.75, -120.44, 3.00) | (-89.22, -23.95, 6.00) | 136.73 |
| 7 | (-184.75, -120.44, 3.00) | (-82.04, -24.33, 6.00) | 142.59 |

**Table 3. Description of the mooring system used in the stress simulation**

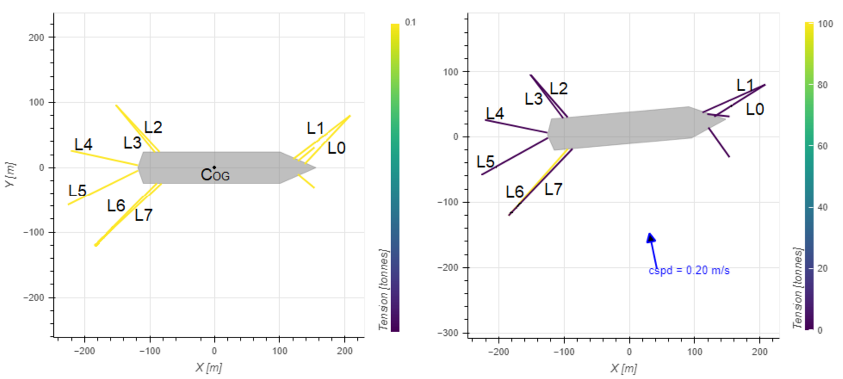


**Figure 12. On the left is the initial layout with the origin at the ship's COG and on the right is the layout at the moment of mooring breakage, where the yellow and purple colors mark the maximum and minimum stress values, respectively.**

The results of the DOFs along the simulation are presented in Figure 13. The first instances of ship movement occur about 9 to 10 hours after the volcano erupts, coinciding with the arrival of atmospheric waves (VMT), with variations in the order of 2 m, 8 m, and 2 degrees for the DOFs Surge, Sway, and Yaw, respectively, in the movements directly associated with tsunami hydrodynamic loads (López and Iglesias, 2014). Then, 15 hours after the eruption, when the 120-minute period wave is present and the mooring breaks, further ship motion is generated, drastically increasing the vessel mentioned above DOFs values. The model results indicate that the movement was caused by the VMT. The anchored ship aligns with the surge, sway, and yaw; with a maximum deviation of 9 meters, 14 meters, and 5 degrees, respectively, which is more than enough to produce the breakage of the mooring system according to the port authority of La Pampilla (CPAAAAE, 2023).

https://doi.org/10.5194/egusphere-2024-663
Preprint. Discussion started: 7 March 2024


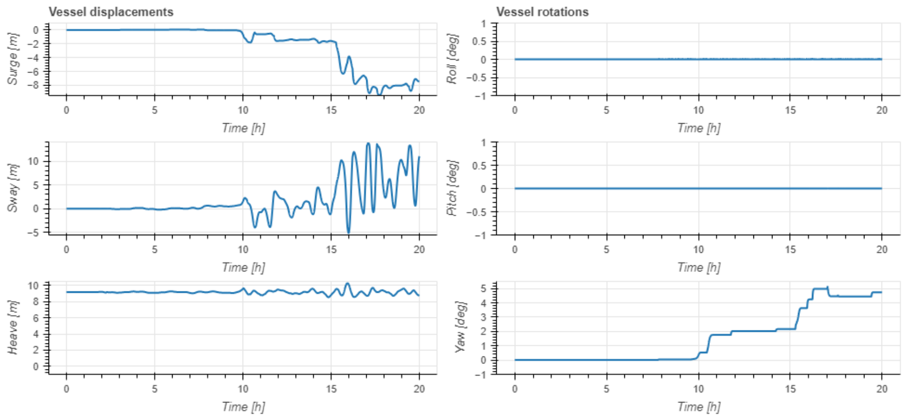


**Figure 13. Time series of ship 6 degrees of freedom obtained from numerical simulation. Measured in hours after the eruption.**

To support the hypothesis that the 120-minute long-period wave along the Peruvian coast caused the mooring to break, a comparison was made between the stresses obtained by forcing with the VMT time-series and the tsunami caused only by the submarine explosion. The stress results for each line in both cases are shown in Figure 14. This illustration shows two things. Firstly, with the VMT, the lines that are primarily under stress are the starboard moorings lines number 0, 4, and 6, the latter having the maximum load (96 tons), which exceeds the Minimum Breaking Load (MBL) by more than 10 tons. The increase in stresses was due to the configuration of the mooring layout, tsunami wave direction, and hydrodynamic effects, which could cause the mooring line to break. Secondly, the findings suggest that the VMT results in a significant increase in mooring stresses, exceeding 10-times the levels observed during the tsunami-only event (where the VMT is not included in the simulation). These results confirm that the atmospheric waves generated during the volcanic eruption have transmitted energy to the ocean, generating tsunami-like waves that have affected the far field.

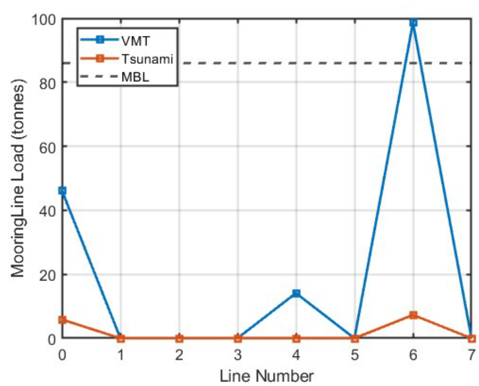


**Figure 14. Maximum stresses obtained from the simulation at each mooring. Blue and orange lines represent the results of the simulations with and without atmospheric waves, respectively.**

https://doi.org/10.5194/egusphere-2024-663
Preprint. Discussion started: 7 March 2024


## 4. Conclusions

The propagation of atmospheric waves and their coupling with the ocean were extensively studied following the Tonga event. Although epistemic uncertainties associated with the event are important, it was possible to understand the main forcers and effects of the volcano-meteorological tsunami (VMT) in the far-field, where the atmospheric waves were the dominant generation mechanism. The air-ocean Proudman resonance in deep water was the driving mechanism that caused sizeable gravity waves, which had very similar characteristics to those of a tectonic-source tsunami.

The potential of the explosion-induced atmospheric waves to magnify tsunamis once they pass over oceanic regions of great depth has become apparent. This happened near the Tonga trench in the propagation direction of South America (Figure 3-c in Omira et al., 2022), helping to understand the origin of long-period tsunami waves propagated toward Peru. The spectral analysis results establish the influence of the atmospheric waves generated by the HTHH volcano.

The presence of the high period waves exclusively in the tide gauges of Peru and Ecuador (**CL** and **LA,** respectively) could be explained by several processes associated with shoaling. These processes could include the width and slope of the continental shelf (which is wider on the Peruvian coast than on the Chilean coast, for example) and the effects associated with topographic boundaries and their geometry, such as the natural bay oscillation modes.

Considering that, the 120-minutes long-period waves were associated with the air-ocean-resonance of the Tonga event and that numerical simulations additionally show the mooring line stress using the VMT time-series, it is possible to conclude that the Tonga tsunami caused the overstressing and subsequent accident in the port of La Pampilla, Peru.

Various processes, including hydrodynamic loads on the ship's hull, can threaten the stability of moored vessels. These loads primarily affect the horizontal plane, which influences the sway, surge, and yaw degrees of freedom. The VMT produced during the Tonga 2022 event was accompanied by long-period waves and currents, which could affect the stability of the mooring system in the port of La Pampilla, Peru.

The hydrodynamic effects that these very long-period waves can cause in port environments can generate damages similar to those of tectonic-source tsunamis, affecting infrastructure, vessels, and merchandise. One unique characteristic of VMT events is that their waves do not dissipate energy with a ratio of $r^{-1/2}$ (where r is the distance from the generation origin). Instead, they can be amplified thousands of kilometers away from their origin, presenting an increased threat to the stability of port environments in the far field.

### 4.1. Final Considerations

Coastal and port infrastructure are not prepared to respond preventively to these Tonga-type tsunamis, leaving them "unprotected", as tsunami warnings are not issued once a volcano eruption is known. Furthermore, in the analyzed event, the initial ocean disturbance arrived earlier than anticipated because the atmospheric waves produced a VMT that travelled at sonic velocity. This statement holds relevance as state and international authorities are responsible for maritime safety and the creation of cautions-warnings and suggestions to aid distinct users in coastal and offshore locations.

This event showed the need for Tsunami Early Warning Systems (TWS) to be prepared to include atmospheric waves and detect them from existing monitoring sensors. In addition, Standard Operational Procedures need to include protocols for these events to avoid damage to port facilities and ships, such as the breaking of moorings and ship collisions. These events can also generate local flooding increasingly far away from the origin and affect the population and coastal infrastructures (cities, nuclear reactors, petrochemical industry, etc.). Therefore, efforts towards the incorporation of tsunamis caused by volcanic acoustic waves in tsunami warning systems are needed.

## 5. Author contribution

Supervision and methodology (G.M and A-Q.I); Waves simulations (K.J and O.R); revision (B.M and O.R). All authors have read and agreed to the published version of the manuscript.

## 6. Competing interests

At least one of the co-authors is a member of the editorial board of Natural Hazards and Earth System Sciences.

## 7. Acknowledgement

This research was supported by an FPU (Formación de Profesorado Universitario) grant from the Spanish Ministry of Science and Innovation (MCINN) to the first author. We have gratitude to The Ocean Energy and Offshore Engineering Group of IHCANTABRIA for the model of mooring stresses. In addition, the authors of this work would like to thank the various state institutions that have provided measured atmospheric data mentioned in Chapter 2: IDEAM (Colombia), SENAMHI (Perú), DGAC (Chile), NIWA (New Zealand), NOAA (USA) and IOC.

## 8. References

Abe, K.: Synthesis of a Tsunami Spectrum in a Semi-Enclosed Basin Using Its Background Spectrum, Pure Appl. Geophys., 168, 1101–1112, https://doi.org/10.1007/s00024-010-0222-x, 2011.

Ana Baptista, M., Miguel Miranda, J., Batlló, J., Lisboa, F., Luis, J., and Maciá, R.: New study on the 1941 Gloria Fault earthquake and tsunami, Nat. Hazards Earth Syst. Sci., 16, 1967–1977, https://doi.org/10.5194/nhess-16-1967-2016, 2016.

Antonopoulos, J.: The great Minoan eruption of Thera volcano and the ensuing tsunami in the Greek Archipelago, Nat. Hazards, 5, 153–168, https://doi.org/10.1007/BF00127003, 1992.

https://doi.org/10.5194/egusphere-2024-663
Preprint. Discussion started: 7 March 2024


Ayca, A. and Lynett, P. J.: Effect of tides and source location on nearshore tsunami-induced currents, J. Geophys. Res. Ocean., 121, 8807–8820, https://doi.org/10.1002/2016JC012435, 2016.

Ayca, A. and Lynett, P. J.: DEBRIS AND VESSEL TRANSPORT DUE TO TSUNAMI CURRENTS IN PORTS AND HARBORS, Coast. Eng. Proc., 68, https://doi.org/10.9753/icce.v36.currents.68, 2018.

Ayca, A. and Lynett, P. J.: Modeling the motion of large vessels due to tsunami-induced currents, Ocean Eng., 236, 109487, https://doi.org/10.1016/j.oceaneng.2021.109487, 2021.

Belousov, A., Voight, B., Belousova, M., and Muravyev, Y.: Tsunamis generated by subaquatic volcanic explosions: Unique data from 1996 Eruption in Karymskoye Lake, Kamchatka, Russia, Pure Appl. Geophys., 157, 1135–1143, https://doi.org/10.1007/s000240050021, 2000.

CPAAAAE: Informe Final sobre las acciones de los funcionarios públicos y privados que ocasionaron el derrame de petróleo de la Empresa Multinacional REPSOL YPF S.A., Lima, 421 pp., 2023.

Dogan, G. G., Yalciner, A. C., Annunziato, A., Yalciner, B., and Necmioglu, O.: Global propagation of air pressure waves and consequent ocean waves due to the January 2022 Hunga Tonga-Hunga Ha'apai eruption, Ocean Eng., 267, 113174, https://doi.org/10.1016/j.oceaneng.2022.113174, 2023.

Dormand, J. R. and Prince, P. J.: A family of embedded Runge-Kutta formulae, J. Comput. Appl. Math., 6, 19–26, https://doi.org/10.1016/0771-050X(80)90013-3, 1980.

Falvard, S., Paris, R., Belousova, M., Belousov, A., Giachetti, T., and Cuven, S.: Scenario of the 1996 volcanic tsunamis in Karymskoye Lake, Kamchatka, inferred from X-ray tomography of heavy minerals in tsunami deposits, Mar. Geol., 396, 160–170, https://doi.org/10.1016/j.margeo.2017.04.011, 2018.

Hamilton, G. D.: National Data Buoy Center Programs, Bull. Am. Meteorol. Soc., 67, 411–415, https://doi.org/10.1175/1520-0477(1986)067<0411:NDBCP>2.0.CO;2, 1986.

Hayward, M. W., Whittaker, C. N., Lane, E. M., Power, W. L., Popinet, S., and White, J. D. L. L.: Multilayer modelling of waves generated by explosive subaqueous volcanism, Nat. Hazards Earth Syst. Sci., 22, 617–637, https://doi.org/10.5194/nhess-22-617-2022, 2022.

Hu, G., Li, L., Ren, Z., and Zhang, K.: The characteristics of the 2022 Tonga volcanic tsunami in the Pacific Ocean, Nat. Hazards Earth Syst. Sci., 23, 675–691, https://doi.org/10.5194/nhess-23-675-2023, 2023.

Hu, Y., Li, Z., Wang, L., Chen, B., Zhu, W., Zhang, S., Du, J., Zhang, X., Yang, J., Zhou, M., Liu, Z., Wang, S., Miao, C., Zhang, L., and Peng, J.: Rapid Interpretation and Analysis of the 2022 Eruption of Hunga Tonga-Hunga Ha̓apai Volcano with Integrated Remote Sensing Techniques, Wuhan Daxue Xuebao (Xinxi Kexue Ban)/Geomatics Inf. Sci. Wuhan Univ. [J], 47, 242–251, https://doi.org/10.13203/J.WHUGIS20220050, 2022.

Imamura, F., Suppasri, A., Arikawa, T., Koshimura, S., Satake, K., and Tanioka, Y.: Preliminary Observations and Impact in Japan of the Tsunami Caused by the Tonga Volcanic Eruption on January 15, 2022, Pure Appl. Geophys., 179, 1549–1560, https://doi.org/10.1007/s00024-022-03058-0, 2022.

Inoue, Y., Rafiqul Islam, M., and Murai, M.: Effect of wind, current and non-linear second order drift forces on a moored multi-body system in an irregular sea, in: Oceans Conference Record (IEEE), 1915–1922, https://doi.org/10.1109/oceans.2001.968139, 2001.

Sea level station monitoring facility: https://www.ioc-sealevelmonitoring.org/station.php?code=call, last access: 1 February 2022.

Journée, J. M. J. and Massie, W. W.: Offshore Hydromechanics, First Edition,

https://doi.org/10.5194/egusphere-2024-663
Preprint. Discussion started: 7 March 2024


https://ocw.tudelft.nl/courses/offshore-hydromechanics/, 2001.

Kienle, J., Kowalik, Z., and Murty, T. S.: Tsunamis generated by eruptions from Mount St. Augustine Volcano, Alaska, https://doi.org/10.1126/science.236.4807.1442, 1987.

Kim, J. and Omira, R.: The 6–7 July 2010 meteotsunami along the coast of Portugal: insights from data analysis and numerical modelling, Nat. Hazards, 106, 1397–1419, https://doi.org/10.1007/s11069-020-04335-8, 2021.

Kim, J., Pedersen, G. K., Løvholt, F., and LeVeque, R. J.: A Boussinesq type extension of the GeoClaw model - a study of wave breaking phenomena applying dispersive long wave models, Coast. Eng., 122, 75–86, https://doi.org/10.1016/j.coastaleng.2017.01.005, 2017.

Kim, J., Choi, B. J., and Omira, R.: On the Greenspan resurgence of meteotsunamis in the Yellow Sea—insights from the newly discovered 11–12 June 2009 event, Nat. Hazards, 114, 1323–1340, https://doi.org/10.1007/s11069-022-05427-3, 2022.

Kirby, J. T., Grilli, S. T., Horrillo, J., Liu, P. L.-F., Nicolsky, D., Abadie, S., Ataie-Ashtiani, B., Castro, M. J., Clous, L., Escalante, C., Fine, I., González-Vida, J. M., Løvholt, F., Lynett, P., Ma, G., Macías, J., Ortega, S., Shi, F., Yavari-Ramshe, S., and Zhang, C.: Validation and inter-comparison of models for landslide tsunami generation, Ocean Model., 170, 101943, https://doi.org/10.1016/j.ocemod.2021.101943, 2022.

Kubota, T., Saito, T., and Nishida, K.: Global fast-traveling tsunamis driven by atmospheric Lamb waves on the 2022 Tonga eruption, Science (80-. )., 377, 91–94, https://doi.org/10.1126/science.abo4364, 2022.

López, M. and Iglesias, G.: Long wave effects on a vessel at berth, Appl. Ocean Res., 47, 63–72, https://doi.org/10.1016/j.apor.2014.03.008, 2014.

Lynett, P., McCann, M., Zhou, Z., Renteria, W., Borrero, J., Greer, D., Fa'anunu, O., Bosserelle, C., Jaffe, B., La Selle, S. P., Ritchie, A., Snyder, A., Nasr, B., Bott, J., Graehl, N., Synolakis, C., Ebrahimi, B., and Cinar, G. E.: Diverse tsunamigenesis triggered by the Hunga Tonga-Hunga Ha'apai eruption, Nature, 609, 728–733, https://doi.org/10.1038/s41586-022-05170-6, 2022.

Lynett, P. J., Borrero, J. C., Weiss, R., Son, S., Greer, D., and Renteria, W.: Observations and modeling of tsunami-induced currents in ports and harbors, Earth Planet. Sci. Lett., 327–328, 68–74, https://doi.org/10.1016/j.epsl.2012.02.002, 2012.

Madsen, P. A. and Sørensen, O. R.: A new form of the Boussinesq equations with improved linear dispersion characteristics. Part 2. A slowly-varying bathymetry, Coast. Eng., 18, 183–204, https://doi.org/10.1016/0378-3839(92)90019-Q, 1992.

Mandli, K. T. and Dawson, C. N.: Adaptive Mesh Refinement for Storm Surge, Ocean Model., 75, 36–50, https://doi.org/10.1016/j.ocemod.2014.01.002, 2014.

Matoza, R. S., Fee, D., Assink, J. D., Iezzi, A. M., Green, D. N., Kim, K., Toney, L., Lecocq, T., Krishnamoorthy, S., Lalande, J. M., Nishida, K., Gee, K. L., Haney, M. M., Ortiz, H. D., Brissaud, Q., Martire, L., Rolland, L., Vergados, P., Nippress, A., Park, J., Shani-Kadmiel, S., Witsil, A., Arrowsmith, S., Caudron, C., Watada, S., Perttu, A. B., Taisne, B., Mialle, P., Le Pichon, A., Vergoz, J., Hupe, P., Blom, P. S., Waxler, R., De Angelis, S., Snively, J. B., Ringler, A. T., Anthony, R. E., Jolly, A. D., Kilgour, G., Averbuch, G., Ripepe, M., Ichihara, M., Arciniega-Ceballos, A., Astafyeva, E., Ceranna, L., Cevuard, S., Che, I. Y., De Negri, R., Ebeling, C. W., Evers, L. G., Franco-Marin, L. E., Gabrielson, T. B., Hafner, K.,

https://doi.org/10.5194/egusphere-2024-663
Preprint. Discussion started: 7 March 2024


Harrison, R. G., Komjathy, A., Lacanna, G., Lyons, J., Macpherson, K. A., Marchetti, E., McKee, K. F., Mellors, R. J., Mendo-Pérez, G., Mikesell, T. D., Munaibari, E., Oyola-Merced, M., Park, I., Pilger, C., Ramos, C., Ruiz, M. C., Sabatini, R., Schwaiger, H. F., Tailpied, D., Talmadge, C., Vidot, J., Webster, J., and Wilson, D. C.: Atmospheric waves and global seismoacoustic observations of the January 2022 Hunga eruption, Tonga, Science (80-. )., 377, 95–100, https://doi.org/10.1126/science.abo7063, 2022.

Tonga Volcanic Eruption & Tsunami: https://appliedsciences.nasa.gov/what-we-do/disasters/disasters-activations/tonga-volcanic-eruption-tsunami-2022, last access: 15 December 2022.

OCIMF: Estimating The Environmental Loads On Anchoring Systems, Oil Companies International Marine Forum, London, 33 pp., 2010.

Oh, M. J., Ham, S. H., and Ku, N.: The coefficients of equipment number formula of ships, J. Mar. Sci. Eng., 8, 1–11, https://doi.org/10.3390/jmse8110898, 2020.

Ohgaki, K., Yoneyama, H., Suzuki, T., and IEEE: Evaluation on safety of moored ships and mooring systems for a tsunami attack, 2008.

Omira, R., Ramalho, R. S., Kim, J., González, P. J., Kadri, U., Miranda, J. M., Carrilho, F., and Baptista, M. A.: Global Tonga tsunami explained by a fast-moving atmospheric source, Nat. 2022 6097928, 609, 734–740, https://doi.org/10.1038/s41586-022-04926-4, 2022.

Pakoksung, K., Suppasri, A., and Imamura, F.: The near-field tsunami generated by the 15 January 2022 eruption of the Hunga Tonga-Hunga Ha'apai volcano and its impact on Tongatapu, Tonga, Sci. Rep., 12, 15187, https://doi.org/10.1038/s41598-022-19486-w, 2022.

Pararas-Carayannis, G.: The tsunami generated from the eruption of the volcano of Santorin in the Bronze Age, Nat. Hazards, 5, 115–123, https://doi.org/10.1007/BF00127000, 1992.

Pararas-Carayannis, G.: Volcanic tsunami generating source mechanisms in the eastern Caribbean region, Sci. Tsunami Hazards, 22, 74–114, 2004.

Paris, R.: Source mechanisms of volcanic tsunamis, Philos. Trans. R. Soc. A Math. Phys. Eng. Sci., 373, https://doi.org/10.1098/rsta.2014.0380, 2015.

Paris, R., Switzer, A. D., Belousova, M., Belousov, A., Ontowirjo, B., Whelley, P. L., and Ulvrova, M.: Volcanic tsunami: A review of source mechanisms, past events and hazards in Southeast Asia (Indonesia, Philippines, Papua New Guinea), https://doi.org/10.1007/s11069-013-0822-8, 7 January 2014.

Proudman, J.: The Effects on the Sea of Changes in Atmospheric Pressure., Geophys. J. Int., 2, 197–209, https://doi.org/10.1111/J.1365-246X.1929.TB05408.X, 1929.

Rabinovich, A. B.: Spectral analysis of tsunami waves: Separation of source and topography effects, J. Geophys. Res. Ocean., 102, 12663–12676, https://doi.org/10.1029/97JC00479, 1997.

Ramírez-Herrera, M. T., Coca, O., and Vargas-Espinosa, V.: Tsunami Effects on the Coast of Mexico by the Hunga Tonga-Hunga Ha'apai Volcano Eruption, Tonga, Pure Appl. Geophys., https://doi.org/10.1007/S00024-022-03017-9, 2022.

Sakakibara, S., Takeda, S., Iwamoto, Y., and Kubo, M.: A hybrid potential theory for predicting the motions of a moored ship induced by large-scaled tsunami, Ocean Eng., 37, 1564–1575, https://doi.org/10.1016/J.OCEANENG.2010.09.005, 2010.

Satake, K., Rabinovich, A. B., Dominey-Howes, D., and Borrero, J. C.: Introduction to "Historical and Recent Catastrophic Tsunamis in the World: Volume I. The 2011 Tohoku Tsunami,"

https://doi.org/10.5194/egusphere-2024-663
Preprint. Discussion started: 7 March 2024


https://doi.org/10.1007/s00024-012-0615-0, 1 June 2013.

Shampine, L. F.: Some Practical Runge-Kutta Formulas, Math. Comput., 46, 135, https://doi.org/10.2307/2008219, 1986.

Shevchenko, G., Shishkin, A., Bogdanov, G., and Loskutov, A.: Tsunami Measurements in Bays of Shikotan Island, Pure Appl. Geophys., 168, 2011–2021, https://doi.org/10.1007/s00024-011-0284-4, 2011.

Shigeki, S. and Masayoshi, K.: Initial attack of large-scaled tsunami on ship motions and mooring loads, Ocean Eng., 36, 145–157, https://doi.org/10.1016/j.oceaneng.2008.09.010, 2009.

SPDA Actualidad Ambiental: https://www.actualidadambiental.pe/derrame-petroleo-cronologia-de-lo-sucedido-segun-el-capitan-del-buque-mare-doricum-video/, last access: 1 March 2024.

Tahar, A. and Kim, M. H.: Hull/mooring/riser coupled dynamic analysis and sensitivity study of a tanker-based FPSO, https://doi.org/10.1016/j.apor.2003.02.001, 2004.

Terry, J. P., Goff, J., Winspear, N., Bongolan, V. P., and Fisher, S.: Tonga volcanic eruption and tsunami, January 2022: globally the most significant opportunity to observe an explosive and tsunamigenic submarine eruption since AD 1883 Krakatau, Geosci. Lett., 9, 24, https://doi.org/10.1186/s40562-022-00232-z, 2022.

Thomson, R. E., Rabinovich, A. B., Fine, I. V., Sinnott, D. C., McCarthy, A., Sutherland, N. A. S., and Neil, L. K.: Meteorological tsunamis on the coasts of British Columbia and Washington, Phys. Chem. Earth, 34, 971–988, https://doi.org/10.1016/j.pce.2009.10.003, 2009.

CNAT: https://www.tvperu.gob.pe/noticias/nacionales/cnat-no-existe-alerta-de-tsunami-en-el-litoral-peruano, last access: 6 February 2022.

World Bank: https://www.worldbank.org/en/news/press-release/2022/02/14/tonga-volcanic-eruption-and-tsunami-world-bank-disaster-assessment-report-estimates-damages-at-us-90m, last access: 28 February 2024.

Wilson, R., Lynett, P., Eskijian, M., Miller, K., LaDuke, Y., Curtis, E., Hornick, M., Keen, A., and Ayca, A.: TSUNAMI HAZARD ANALYSIS AND PRODUCTS FOR HARBORS IN CALIFORNIA, in: Tsunami Hazards: Innovations in Mapping, Modeling, and Outreach, https://doi.org/10.1130/abs/2017am-306344, 2017.

Wright, C. J., Hindley, N. P., Alexander, M. J., Barlow, M., Hoffmann, L., Mitchell, C. N., Prata, F., Bouillon, M., Carstens, J., Clerbaux, C., Osprey, S. M., Powell, N., Randall, C. E., and Yue, J.: Surface-to-space atmospheric waves from Hunga Tonga–Hunga Ha'apai eruption, Nature, 609, 741–746, https://doi.org/10.1038/s41586-022-05012-5, 2022.

Xu, Z., Sun, L., Rahman, M. N. A., Liang, S., Shi, J., and Li, H.: Insights on the small tsunami from January 28, 2020, Caribbean Sea MW7.7 earthquake by numerical simulation and spectral analysis, Nat. Hazards, 111, 2703–2719, https://doi.org/10.1007/s11069-021-05154-1, 2022.

Yokoyama, I.: A geophysical interpretation of the 1883 Krakatau eruption, J. Volcanol. Geotherm. Res., 9, 359–378, https://doi.org/10.1016/0377-0273(81)90044-5, 1981.

Zheng, Z., Ma, X., Yan, M., Ma, Y., and Dong, G.: Hydrodynamic response of moored ships to seismic-induced harbor oscillations, Coast. Eng., 176, 104147, https://doi.org/10.1016/j.coastaleng.2022.104147, 2022.